

A general strategy for preparing pyrrolic-N₄ type single-atom catalysts *via* pre-located isolated atoms

Junjie Li^{1,8}, Ya-fei Jiang^{2,8}, Qi Wang^{3,8}, Cong-Qiao Xu ², Duojie Wu³, Mohammad Norouzi Banis ¹, Keegan R. Adair¹, Kieran Doyle-Davis¹, Debora Motta Meira ^{4,5}, Y. Zou Finrock^{4,5}, Weihan Li¹, Lei Zhang¹, Tsun-Kong Sham ⁶, Ruying Li¹, Ning Chen ⁴✉, Meng Gu ³✉, Jun Li^{2,7}✉ & Xueliang Sun ¹✉

Single-atom catalysts (SACs) have been applied in many fields due to their superior catalytic performance. Because of the unique properties of the single-atom-site, using the single atoms as catalysts to synthesize SACs is promising. In this work, we have successfully achieved Co₁ SAC using Pt₁ atoms as catalysts. More importantly, this synthesis strategy can be extended to achieve Fe and Ni SACs as well. X-ray absorption spectroscopy (XAS) results demonstrate that the achieved Fe, Co, and Ni SACs are in a M₁-pyrrolic N₄ (M= Fe, Co, and Ni) structure. Density functional theory (DFT) studies show that the Co(Cp)₂ dissociation is enhanced by Pt₁ atoms, thus leading to the formation of Co₁ atoms instead of nanoparticles. These SACs are also evaluated under hydrogen evolution reaction (HER) and oxygen evolution reaction (OER), and the nature of active sites under HER are unveiled by the *operando* XAS studies. These new findings extend the application fields of SACs to catalytic fabrication methodology, which is promising for the rational design of advanced SACs.

¹Department of Mechanical and Materials Engineering, University of Western Ontario, London, ON N6A 5B9, Canada. ²Department of Chemistry, Southern University of Science and Technology, 518055 Shenzhen, China. ³Department of Materials Science and Engineering, Southern University of Science and Technology, 518055 Shenzhen, China. ⁴Science Division, Canadian Light Source Inc., 44 Innovation Boulevard, Saskatoon, SK S7N 2V3, Canada. ⁵CLS @ APS, Advanced Photon Source, Argonne National Laboratory, Lemont, IL 60439, USA. ⁶Department of Chemistry, University of Western Ontario, London, ON N6A 5B7, Canada. ⁷Department of Chemistry and Key Laboratory of Organic Optoelectronics and Molecular Engineering of Ministry of Education, Tsinghua University, 100084 Beijing, China. ⁸These authors contributed equally: Junjie Li, Ya-fei Jiang, Qi Wang. ✉email: ning.chen@lightsource.ca; gum@sustech.edu.cn; junli@tsinghua.edu.cn; xsun9@uwo.ca

Single-atom catalysts (SACs)¹ have attracted considerable interest due to their superior catalytic activity and unique selectivity towards different chemical reactions, including CO oxidation^{1,2}, hydrogenation³, dehydrogenation^{4,5}, and electrochemical reactions^{6–8}. Recently, the application of SACs has been widely extended to various research areas^{9–14} including energy storage systems like Li-S batteries¹⁵, enzyme catalysis¹⁶, photocatalysis¹⁷, and even cellular NO sensor¹⁸. Therefore, SACs are continuously showing great potentials for wide applications.

The most significant distinction between SACs and other types of catalysts is their unique single-atom-site, which both increases the atom utilization efficiency and tailors the interaction between the reactant and metal atoms through the adsorption and activation process. For example, Yan et al. reported the Pd₁/graphene SACs showed a high butane selectivity in the hydrogenation of 1,3-butadiene, where the adsorption of 1,3-butadiene on Pd₁ was mainly in a mono- π mode, which differs from that on Pd bulk³. Duchesne and co-workers showed that the Pt single atoms on Au nanoparticles (NPs) exhibited superior catalytic performance in formic acid oxidation. Such a high activity of Pt₄Au₉₆ is ascribed to the weakened CO adsorption on single and few Pt atoms than that on Pt bulk¹⁹. Li and co-workers demonstrated that the Pt₁/Co₃O₄ exhibited a much weaker H₂ adsorption energy than Pt bulk, thus leading to its high catalytic performance in the dehydrogenation of ammonia borane⁵.

However, because of their highly un-saturated coordination environment, heterogeneously supported single atoms possess a dramatically increased surface-free energy, which can lead to their aggregation into NPs, particularly at high metal loadings. Recently, some strategies have been developed to achieve relatively high-loading SACs. These methods include zeolite or mesoporous carbon to stabilize single atoms through a confinement strategy^{20–23}, metal-organic frameworks (MOFs) to achieve SACs through high-temperature pyrolysis²⁴, metal NPs to achieve SACs through high-temperature migration^{25,26}, and a high-temperature shock wave treatment to achieve high loading SACs²⁷. However, there are yet some restrictions on these newly developed methods such as general applicability. Therefore, developing a general approach for the synthesis of various types of SACs is highly desired.

Atomic layer deposition (ALD), a sequential surface reaction relying on a self-limiting process is used to synthesize non-noble single atoms such as Fe and Co^{28,29}. Unfortunately, it results in a low metal loading and the formation of NPs, especially on carbon-based supports due to the high dissociation barrier and predominantly physical adsorption of metal precursors^{28–31}. Therefore, a new reasonable route to produce SACs by ALD may be achieved by lowering the dissociation energy of the ALD precursor. For instance, this high dissociation energy might be strongly reduced on a metal surface^{31–33}. Accordingly, the use of metal single atoms as the catalyst to facilitate the dissociation of ALD precursors to synthesize SACs would be very promising. To the best of our knowledge, this new SACs producing strategy that uses surface single atoms as the catalysts has never been reported. Moreover, the ALD method is feasible to obtain single atoms on various supports, which not only provides a new way to achieve SACs with dual atomic sites but also extends the application fields of SACs to the catalytic fabrication methodology.

In this work, we firstly verified the strategy by using supported Pt single atoms on N-doped carbon nanosheets (Pt₁/NCNS) as the catalyst to synthesize Co SAC through ALD. X-ray absorption spectroscopy (XAS) results reveal singly dispersed Co₁ atoms. Interestingly, the Pt₁ atoms are still atomically dispersed after Co deposition, as confirmed by XAS and high-angle annular dark-field scanning transmission electron microscopy (HAADF-STEM). Furthermore, we also show that this synthesis strategy is

general and can also be easily extended to achieve Fe and Ni SACs. X-ray absorption near edge structure (XANES) simulation and extended X-ray absorption fine structure (EXAFS) analysis results demonstrate that the achieved Co, Fe, and Ni SACs are in a M₁-pyrrolic-N₄ structure (M=Fe, Co, and Ni). Density functional theory (DFT) calculations show that Pt₁ atoms promote the dissociation of Co(Cp)₂ into CoCp and Cp fragments. The Co(Cp) product further deposited on the substrate through strong chemisorption, thus leading to a higher metal loading and formation of Co₁ atoms. These SACs were evaluated under hydrogen evolution reaction (HER) and the nature of single-atom sites are unveiled by the *operando* XAS studies. Moreover, in the oxygen evolution reaction (OER), the Ni₁ SAC showed much higher activity than Fe₁ and Co₁ SACs, which is in line with the DFT predictions.

Results and discussion

Direct fabrication of Pt and Co single atoms on NCNS using ALD. Graphene like NCNS (Fig. 1a and Supplementary Fig. 1) was firstly achieved using C₃N₄ as the template and glucose as the carbon source³⁴. N K-edge XANES results indicate that there are various types of N species including pyridinic, pyrrolic, and graphitic N on NCNS (Fig. 1b)³⁵. According to the literature, the N defects can coordinate with metal species and form a stable SAC⁷. Therefore, the NCNS substrate shows high potential for the synthesis of SACs. After performing one cycle of Pt ALD on NCNS, well-dispersed Pt single atoms were confirmed by HAADF-STEM (Supplementary Fig. 2) and XAS results (Supplementary Fig. 3)³⁶. The loading of Pt is as high as 2.0 wt% based on the inductively coupled plasma optical emission spectrometer (ICP-OES) results.

Since the NCNS shows great potential to support Pt₁ atoms, it has the possibility to act as a suitable substrate for other types of SACs. Using ALD, we performed one cycle of Co ALD on NCNS with Co(Cp)₂ and O₂ as the precursors. However, unlike the formation of Pt₁ atoms, we found obvious Co NPs/clusters in HAADF-STEM (Supplementary Fig. 4a) and Co-Co coordination from the EXAFS results at the Co K edge (Fig. 1c), indicating the formation of Co NPs (Co-NPs/NCNS). Besides the formation of Co NPs, we also noticed a very low metal loading of Co (0.5 wt%). Such a low loading of Co indicates limited physisorption after the dose of Co(Cp)₂ precursor, and the unreacted Co(Cp)₂ would be purged away by N₂ as illustrated in (Supplementary Fig. 5), leading to a low effective Co deposition³⁰. Unfortunately, the weak adsorption effect of Co(Cp)₂ on NCNS will form Co NPs due to the weak interaction between Co species and substrate when O₂ is introduced. Therefore, the direct utilization of the Co ALD process to produce Co single atoms on NCNS is not practical.

Synthesizing Co, Fe, and Ni SACs using pre-located isolated Pt₁ atoms. Inspired by previous research, the dissociation of Co(Cp)₂ will be enhanced on the metal surface³⁷. In our system, the Pt single atoms are easy to achieve, and the Pt-based catalysts are active in many chemical reactions. Therefore, the singly dispersed Pt₁ atoms may have a similar ability and are likely capable to decrease the dissociation energy of Co(Cp)₂, which may increase the Co loading and more importantly to achieve Co single atoms. With this idea in mind, we firstly conducted one cycle of Pt ALD on NCNS to achieve Pt₁/NCNS and followed up with one cycle of Co ALD to verify our assumption (Fig. 1d). After performing one cycle of Co ALD on Pt₁/NCNS substrate, the Co K edge EXAFS of this sample exhibits only one single peak at 1.57 Å (Fig. 2a), which can be attributed to the first shell of Co-C/N/O coordination. Meanwhile, the coordination of Co-Co is

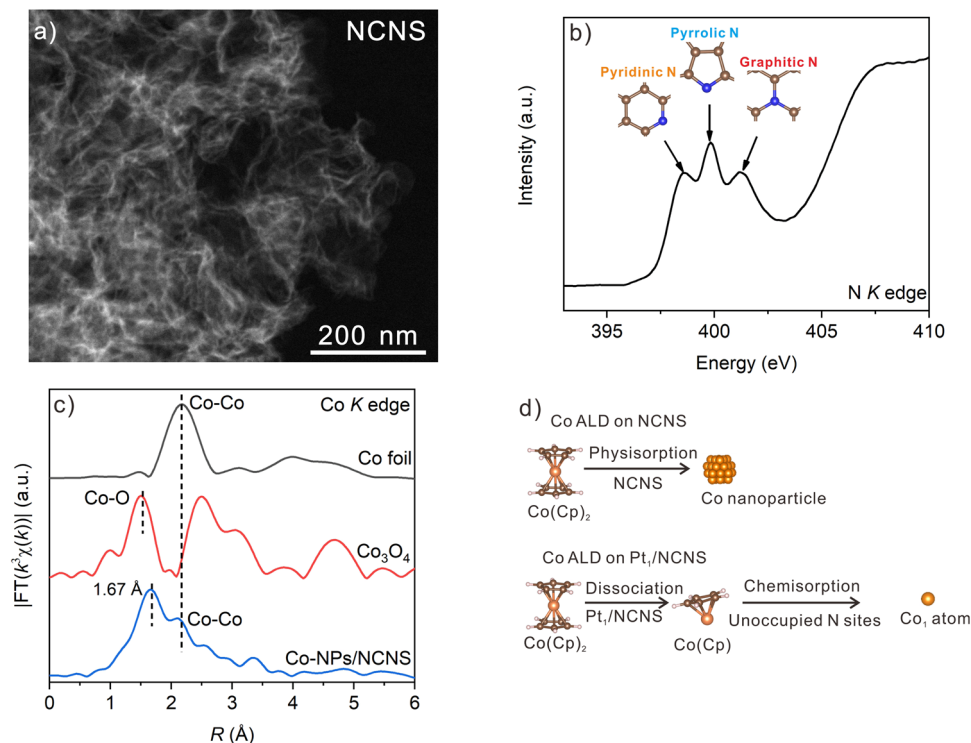


Fig. 1 Characterizations for pristine NCNS, Co-NPs/NCNS, and proposed synthesis strategies for Co SAC. **a** HAADF-STEM image of NCNS. **b** XANES of NCNS at N K edge. **c** FT-EXAFS of Co-NPs/NCNS, as well as Co foil and Co_3O_4 reference at Co K edge, respectively. **d** Assumption of the Co ALD process on pristine NCNS and Pt_1/NCNS . The white, brown, blue, and orange spheres represent H, C, N, and Co, respectively.

negligible, indicating that the Co species mostly exist as single atoms from the new synthesis strategy. In the following parts, this sample is denoted as $\text{Co}_1\text{Pt}_1/\text{NCNS}$.

In order to further extend the application of this synthesis strategy to other SACs such as Fe and Ni, we have chosen to use Fe and Ni ALD precursors with similar chemical structures as that of Co, i.e., ferrocene and nickelocene, respectively. Similarly, Fe and Ni single atoms also cannot be achieved by ALD on pristine NCNS as revealed by Fe-Fe and Ni-Ni coordination in the EXAFS (Fig. 2b, c) and TEM results (Supplementary Fig. 4). In contrast, the Fe-Fe and Ni-Ni coordination are significantly depressed when performing one cycle of Fe and Ni ALD on Pt_1/NCNS ($\text{Fe}_1\text{Pt}_1/\text{NCNS}$ and $\text{Ni}_1\text{Pt}_1/\text{NCNS}$) (Fig. 2b, c). Wavelet-transform EXAFS results further verified the atomically dispersed Co, Fe, and Ni single atoms, which differs from that of their foil and oxide (Fig. 2d, f).

More interestingly, the Pt L_3 edge XANES (Fig. 2g) and X-ray Photoelectron Spectroscopy (XPS) (Supplementary Fig. 6) results show inconspicuous differences, indicating the electronic properties of Pt on these $\text{M}_1\text{Pt}_1/\text{NCNS}$ ($\text{M}=\text{Fe}$, Co, and Ni) samples are close to that on Pt_1/NCNS . Pt L_3 edge EXAFS results further confirm the stable local structure of the Pt_1 atom (Fig. 2h). Typical EXAFS fitting on $\text{Co}_1\text{Pt}_1/\text{NCNS}$ at Pt L_3 edge also demonstrates the unchanged atomic nature of Pt single atoms (Supplementary Fig. 7 and Supplementary Table 1). These results indicate that the Pt_1 atoms are still atomically dispersed after the deposition of Co, Fe, and Ni. This observation provides strong evidence that the Pt_1 atoms only act as the catalyst, while they change the deposition process of Co, Fe, and Ni, but does not lose the atomic dispersion or form a Pt-Co/Fe/Ni cluster, because of the lack of metal-metal coordination in Pt L_3 , Fe, Co, and Ni K edges EXAFS results. Subsequently, we examined the Co loading through ICP-OES after performing one cycle of Co ALD on pristine NCNS and Pt_1/NCNS (Fig. 2i). The ICP-OES results

show that the Co loading of $\text{Co}_1\text{Pt}_1/\text{NCNS}$ (1.8 wt%) is more than three times higher than that of Co-NPs/NCNS (0.5 wt%). Similar results are also observed on Fe and Ni, showing low Fe and Ni loadings on Fe-NPs/NCNS and Ni-NPs/NCNS (0.6 and 0.5 wt%) but much higher on $\text{Fe}_1\text{Pt}_1/\text{NCNS}$ and $\text{Ni}_1\text{Pt}_1/\text{NCNS}$ (1.6 and 2.2 wt%), respectively. These results unambiguously demonstrate that the Pt_1 atoms change the adsorption model of M precursors to predominantly chemisorption, which promotes the degree of effective deposition. However, when the M ALD was performed on pristine NCNS, physisorption is dominant, thus leading to a low metal loading because of less effective deposition.

Morphology of $\text{M}_1\text{Pt}_1/\text{NCNS}$ catalysts. The morphology of $\text{M}_1\text{Pt}_1/\text{NCNS}$ catalysts is characterized by HAADF-STEM. As shown in Fig. 3a, e, i, no observable Pt or M NPs can be found at low magnification. Energy dispersive X-ray (EDX) mapping results show the Pt and M elements are well-dispersed on the NCNS substrate (Fig. 3b, f, j and Supplementary Figs. 8 to 10), indicating their uniform dispersion and high density. At high magnification, high-density bright Pt single atoms (white circles) can be found on $\text{Co}_1\text{Pt}_1/\text{NCNS}$ (Fig. 3c and Supplementary Fig. 8f), $\text{Fe}_1\text{Pt}_1/\text{NCNS}$ (Fig. 3g and Supplementary Fig. 9f), and $\text{Ni}_1\text{Pt}_1/\text{NCNS}$ (Fig. 3k and Supplementary Fig. 10f). All the visible Pt atoms are singly dispersed without any obvious clusters or NPs. Meanwhile, some isolated atoms with less brightness (red circles) were also found to reside nearby the bright Pt_1 atoms, which can be assigned to Fe, Co, and Ni single atoms due to their lower Z-contrast. Furthermore, when the electron energy loss spectroscopy (EELS) was measured at the atoms with less brightness on $\text{Co}_1\text{Pt}_1/\text{NCNS}$, the signals of Co L_2 and L_3 could also be detected (Fig. 3d), confirming the existence of Co_1 atoms. Similar results can be also found on $\text{Fe}_1\text{Pt}_1/\text{NCNS}$ (Fig. 3h) and $\text{Ni}_1\text{Pt}_1/\text{NCNS}$ (Fig. 3i). Based on the HAADF-STEM results, the

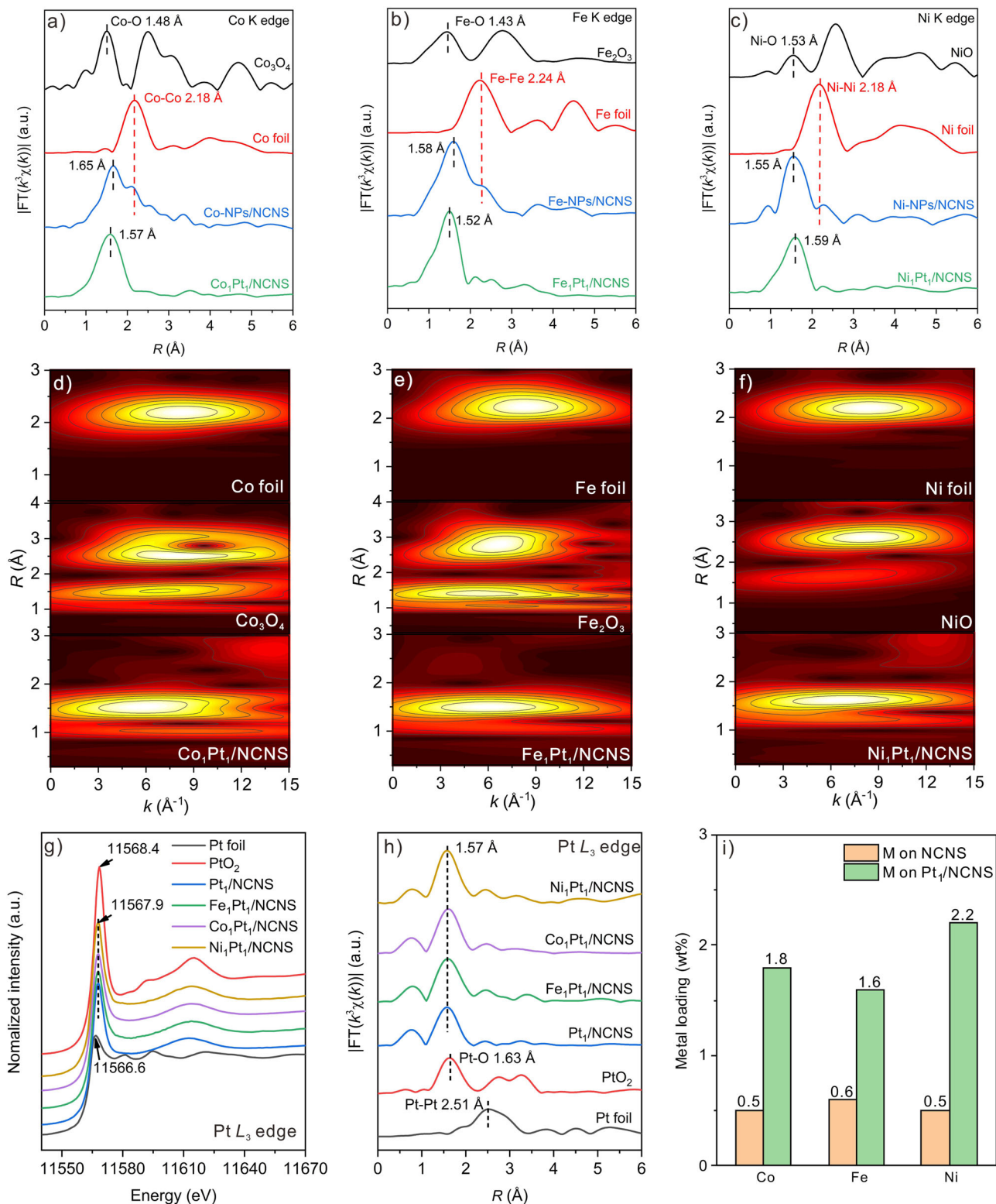


Fig. 2 XAS characterizations for $M_1Pt_1/NCNS$ catalysts. **a-c** Radial distribution curve from FT-EXAFS of Co-NPs/NCNS, Co₁Pt₁/NCNS, Fe-NPs/NCNS, Fe₁Pt₁/NCNS, Ni-NPs/NCNS, and Ni₁Pt₁/NCNS, respectively, as well as their corresponding foil and oxide reference at Co, Fe, and Ni K edges. **d-f** Wavelet-transformed spectra of Co₁Pt₁/NCNS, Fe₁Pt₁/NCNS, Ni₁Pt₁/NCNS, as well as their corresponding foil and oxide reference at Co, Fe, and Ni K edges. **g** and **h** XANES and FT-EXAFS of Pt₁/NCNS, Co₁Pt₁/NCNS, Fe₁Pt₁/NCNS, and Ni₁Pt₁/NCNS, respectively, as well as Pt foil and PtO₂ reference at Pt L₃ edge. **i** ICP-OES results of M (Fe, Co, and Ni) metal loadings.

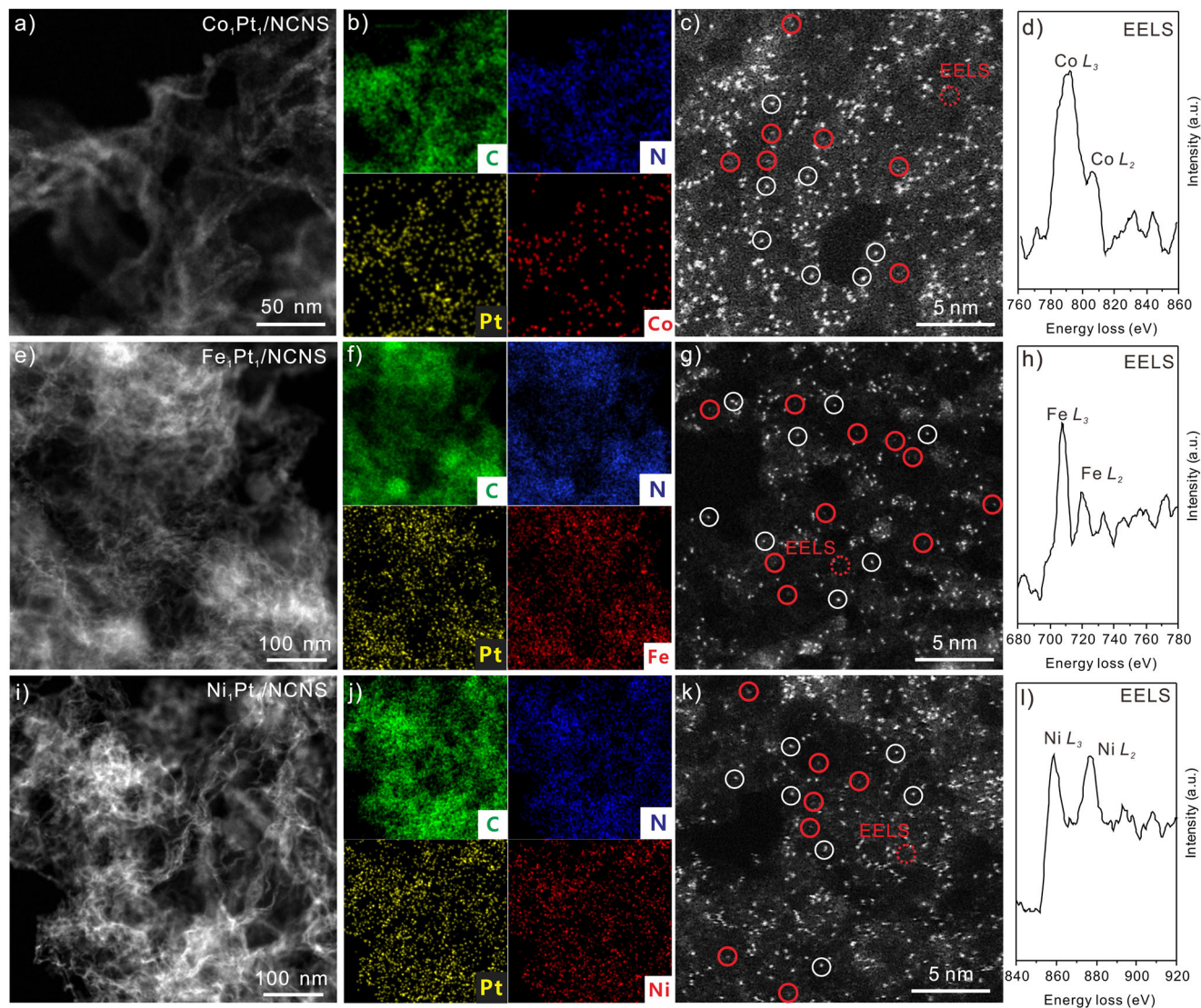


Fig. 3 Morphology of $M_1Pt_1/NCNS$ catalysts. HAADF-STEM images of $Co_1Pt_1/NCNS$ (**a**), $Fe_1Pt_1/NCNS$ (**e**), and $Ni_1Pt_1/NCNS$ (**i**) at low resolution and corresponding EDX mapping (**b**, **f**, and **j**). HAADF-STEM images on $Co_1Pt_1/NCNS$ (**c**), $Fe_1Pt_1/NCNS$ (**g**), and $Ni_1Pt_1/NCNS$ (**k**) samples. The white circles highlight the Pt single atoms. The red circles highlight the Co, Fe, and Ni single atoms, respectively. **d**, **h**, and **l** Corresponding EELS spectra at the location of red dash circle in **c**, **g**, and **k**.

Fe, Co, and Ni-Pt pairs are absent. Taken together, the EXAFS and HAADF-STEM results demonstrate the single-atom nature of both Pt and M atoms on NCNS.

Structure identification of M SACs. Using this synthesis strategy, we have successfully achieved Co, Fe, and Ni SACs. Unveiling the local structure of these SACs is critical to understand the synthesis mechanism and their catalytic applications. XANES spectroscopy is very sensitive to the local geometric structure of the photon-absorbing atom, which provides a better option to understand the local atomic structure. As shown in Fig. 4a to c, the $Co_1Pt_1/NCNS$, $Fe_1Pt_1/NCNS$, and $Ni_1Pt_1/NCNS$ at Co, Fe, and Ni *K* edge XANES spectra, respectively, show significant differences from their corresponding foil and oxide references. We also notice that the XANES spectra of $Co_1Pt_1/NCNS$, $Fe_1Pt_1/NCNS$, and $Ni_1Pt_1/NCNS$ are nearly identical, indicating a similar local coordination environment of $M_1Pt_1/NCNS$ catalysts. This can be delineated since the *k*-dependent absorber phase shift of Fe, Co, and Ni, adjacent in the periodic

table, is very similar. Taking the first derivative XANES of $M_1Pt_1/NCNS$, the energy position of the point of first inflection suggests that the oxidation states of Fe, Co, and Ni are close to +3, +2, and +2, respectively. These observations are perfectly in line with the XPS results (Supplementary Fig. 11).

Focusing on the $Co_1Pt_1/NCNS$ catalyst, we first compared the modeling XANES result based on a recently reported $Co-C_4-O_2$ type Co_1 atom on graphene using ALD (Supplementary Fig. 12a)³⁸. Significant differences can be observed between the theoretical simulated XANES and experimental results, indicating the necessity to consider the critical role of N atoms. We then further compared the reported pyridinic- N_4 -based Co_1-N_4 structure, which still shows the obvious difference with our experimental XANES results (Supplementary Fig. 12b), suggesting the existence of defects in this model as well. Then we progressively add one and two end-on oxygen moieties along the axial direction of the pyridinic Co_1-N_4 structure (Supplementary Fig. 12c, d). Although parts of the experimentally resolved features can be reproduced and achieve a satisfactory agreement with the $Co_1Pt_1/NCNS$ Co *K* edge XANES results, the short Co-N

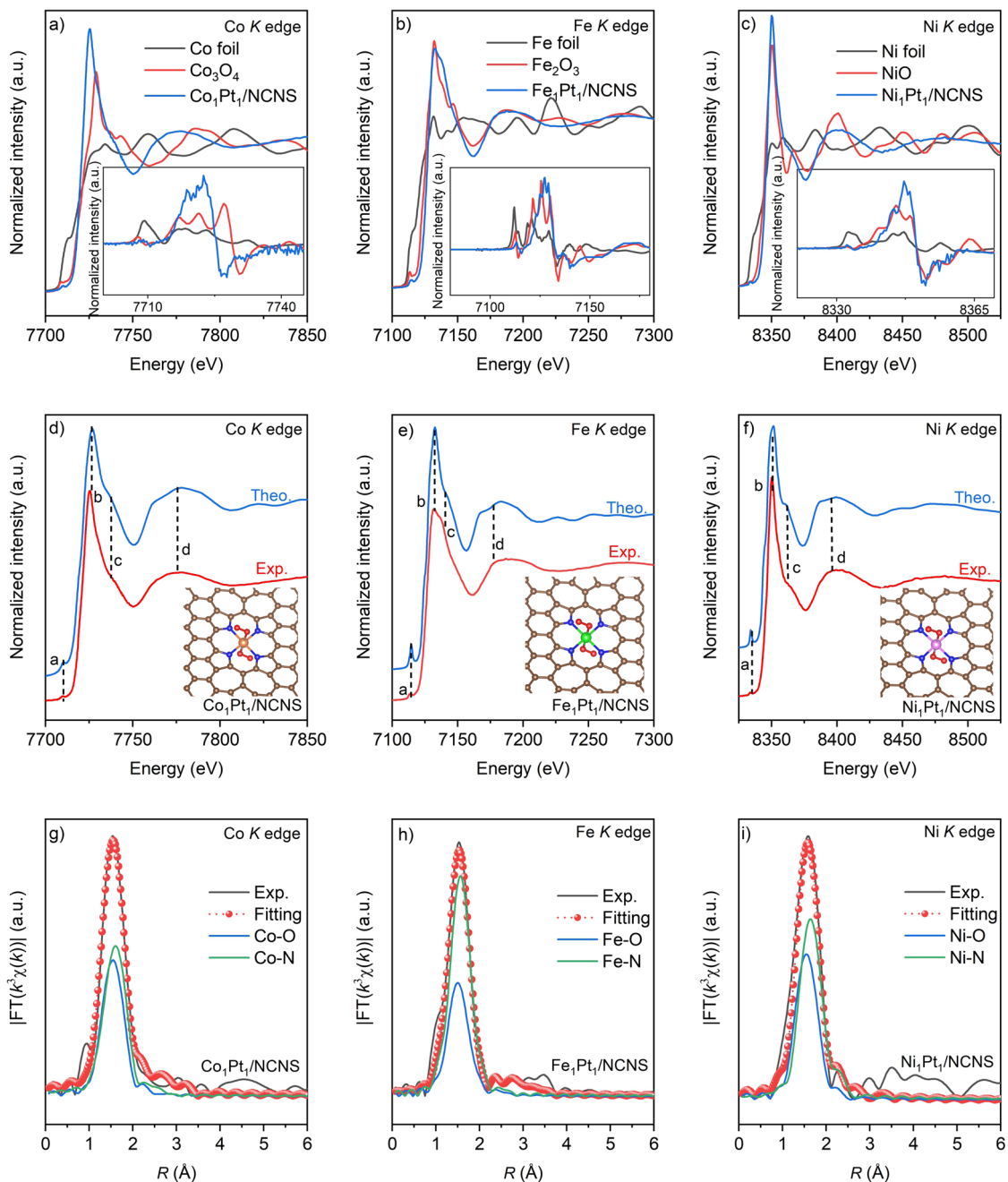


Fig. 4 Identification of the local structure of $M_1Pt_1/NCNS$ catalysts. **a–c** The experimental K-edge XANES spectra and first derivative curves (insets) of $M_1Pt_1/NCNS$ and references samples. **d–f** Comparison between the experimental K-edge XANES spectra of $M_1Pt_1/NCNS$ and the simulated spectra. Some of the main features reproduced are highlighted at points “a” to “d”. Fitting results of the k^3 -weighted FT spectrum of $M_1Pt_1/NCNS$ at Co (**g**), Fe (**h**), and Ni (**i**) K edges. The white, brown, blue, red, orange, green, and pink spheres represent H, C, N, O, Co, Fe, and Ni, respectively.

bonding distance (less than 1.90 Å) disagrees with our EXAFS results (Fig. 2a). Considering that there is a large proportion of pyrrolic-N in the NCNS support, the possibility of a pyrrolic- N_4 type Co_1-N_4 structure cannot be ruled out. As shown in Supplementary Fig. 12e, the simulated XANES result of pyrrolic- N_4 -based Co_1-N_4 showed much better conformity than the pyridinic- N_4 structure. We then further added one molecule of dioxygen with end on coordination on Co_1 atom, the features from “b” to “d” are well reproduced but the pre-edge feature “a” is exaggerated (Supplementary Fig. 12f). However, when we added another molecule of dioxygen on the Co_1 atom at the opposite side, all the features from “a” to “d” can be correctly reproduced (Fig. 4d). Similarly, the simulated $2O_2-Fe_1$ -pyrrolic N_4 and $2O_2-$

Ni_1 -pyrrolic N_4 XANES spectra (Fig. 4e, f) show the most satisfactory results comparing with other DFT optimized structures (Supplementary Figs. 13 and 14). It is important to note, this is the first time that general M_1 -pyrrolic N_4 type SACs can be achieved using ALD, as this type of SACs is usually achieved through high-temperature pyrolysis and ball-milling methods^{39,40}. Besides the above XANES simulation, we also carried out the EXAFS fitting and the results consistently demonstrate the $2O_2-M_1$ -pyrrolic N_4 moiety (Fig. 4g to i, Supplementary Figs. 15 to 18, and Table 1). It is worth noting that the EXAFS results perfectly match the DFT results (Supplementary Table 2). In summary, a close local structure of $Co_1Pt_1/NCNS$, $Fe_1Pt_1/NCNS$ and $Ni_1Pt_1/NCNS$ from simulated

XANES and EXAFS fitting results strongly suggest the same deposition mechanism for Co, Fe, and Ni ALD on Pt₁/NCNS, which indicates that this synthesis strategy can be a universal approach to achieve M₁-pyrrolic N₄ type SACs using Pt₁ atoms.

Theoretical understanding of deposition process. Having resolved the structures of M₁Pt₁/NCNS and Pt₁/NCNS, we carried out DFT calculations to elucidate the deposition mechanism. Considering the similar structure of Co, Fe, and Ni ALD precursors and local structures of Co₁Pt₁/NCNS, Fe₁Pt₁/NCNS, and Ni₁Pt₁/NCNS catalysts, typical Co ALD process is chosen for the following theoretical investigation. As revealed by the calculated Gibbs free energies shown in Fig. 5a, the Co(Cp)₂ has moderate

adsorption ($\Delta G_{\text{ad}} = -0.32$ eV) but very high dissociation energy ($\Delta G_{\text{de}} = 4.91$ eV) on the pristine NCNS. Therefore, the physisorption of Co(Cp)₂ should be dominant on pristine NCNS. This physically and weakly adsorbed Co(Cp)₂ will lead to a low metal loading from inefficient deposition (Fig. 2i and Supplementary Fig. 5). Owing to the weak physisorption, Co species will easily aggregate because of the lack of strong chemical bonding with the substrate. Therefore, Co NPs were observed in the direct Co ALD process on NCNS (Fig. 1c). However, when Pt₁ atoms are involved in the Co ALD process, the deposition model differs considerably. Although the adsorption of Co(Cp)₂ on Pt₁ atom is slightly weaker ($\Delta G_{\text{ad}} = +0.06$ eV), the dissociation energy of Co(Cp)₂ is reduced to $\Delta G_{\text{de}} = 3.54$ eV. The lower dissociation energy can be attributed to the electron transfer from the Cp ligand to the Pt₁/NCNS, thus weakening the interactions between Co and Cp, which facilitates the dissociation process (Supplementary Fig. 19 and Supplementary Table 3). Considering it is a gas phase reaction, the Co(Cp) likely diffuses and deposits on the unoccupied pyrrolic N₄ sites through chemisorption. Such a strong chemical bonding of Co with pyrrolic N₄ sites will form a stable Co₁ structure after the O₂ pulse to remove the Cp ligand. It is worth noting that the introduction of O₂ may also remove the attached Cp ligand on the Pt₁ atom and recover the structure of Pt₁/NCNS as shown in the Pt L₃ XANES and EXAFS results (Fig. 2g, h). As a result, when the Co ALD is performed on Pt₁/NCNS, Co single atoms will form and Pt₁ atoms will remain atomic dispersion (Fig. 5b). The principle revealed by the theoretical calculation results indicates that this synthesis strategy could be universal for the rational design of SACs (Supplementary Fig. 20).

Theoretical simulation and electrocatalytic performance of M₁Pt₁/NCNS. The capability of application for the achieved M₁Pt₁/NCNS catalysts was further evaluated in electrochemical reactions. Prior to the experiment, we first studied the projected

Table 1 Structural parameters of the M₁Pt₁/NCNS (M=Fe, Co, and Ni), foil, and oxide references extracted from quantitative EXAFS curve-fittings at Co, Fe, and Ni K edges.

Sample	Path	CNs	R (Å)	σ^2 (10 ⁻³ Å ²)	ΔE_0 (eV)
Co foil	Co-Co	12.0	2.49	6.1	6.9
Co ₃ O ₄	Co-O	4.0	1.91	1.7	1.0
Co ₁ Pt ₁ /NCNS	Co-O	2.0	1.98	3.3	2.2
NCNS	Co-N	4.0	2.08	6.4	
Fe foil	Fe-Fe	8.0	2.46	5.3	5.3
	Fe-Fe	6.0	2.85		
Fe ₂ O ₃	Fe-O	6.0	1.93	10.0	-6.0
Fe ₁ Pt ₁ /NCNS	Fe-O	2.2	1.95	2.0	-4.2
NCNS	Fe-N	4.2	2.02	2.9	
Ni foil	Ni-Ni	12.0	2.48	6.1	7.4
NiO	Ni-O	6.0	2.05	4.2	-3.7
Ni ₁ Pt ₁ /NCNS	Ni-O	2.2	1.99	1.5	2.1
NCNS	Ni-N	4.2	2.11	2.5	

CNs coordination numbers, R bonding distance, σ^2 Debye-Waller factor, ΔE_0 inner potential shift. Errors in the fitting parameters are CN \pm 20%, R \pm 0.02, σ^2 \pm 20%, and ΔE_0 \pm 3.0.

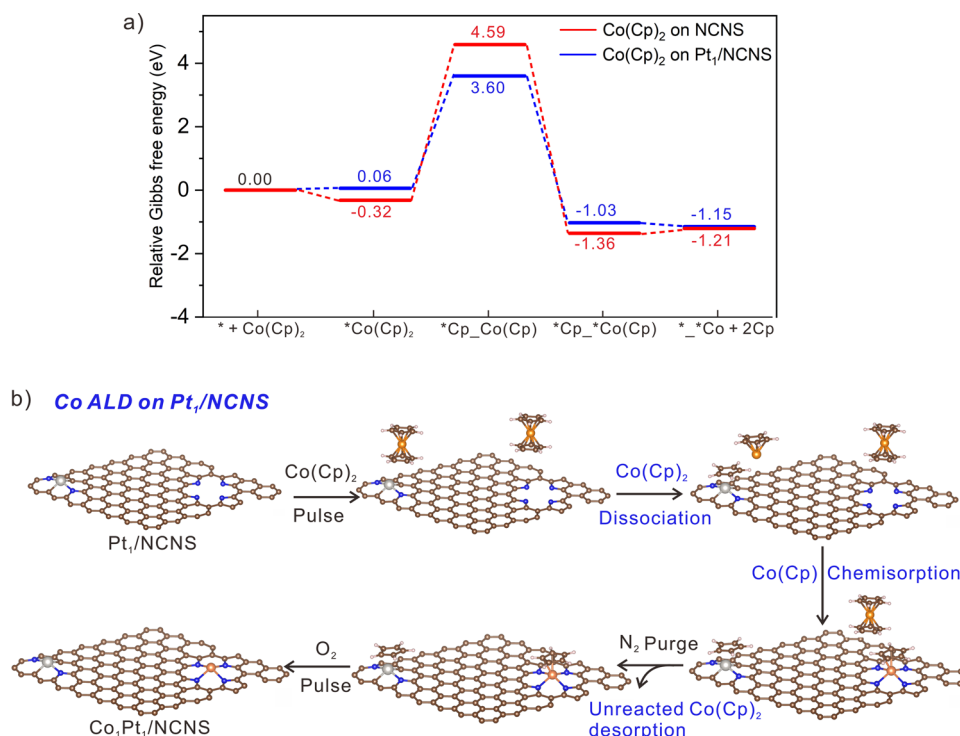


Fig. 5 Illustration of theoretical understanding of the Co ALD process. **a** Theoretical reaction coordinate for Co(Cp)₂ deposition on pristine NCNS and Pt₁/NCNS. The Gibbs free energies were calculated at T = 523 K and P = 1 atm. **b** Illustration of Co ALD process on Pt₁/NCNS. The white, brown, blue, orange, and silver spheres represent H, C, N, Co, and Pt, respectively.

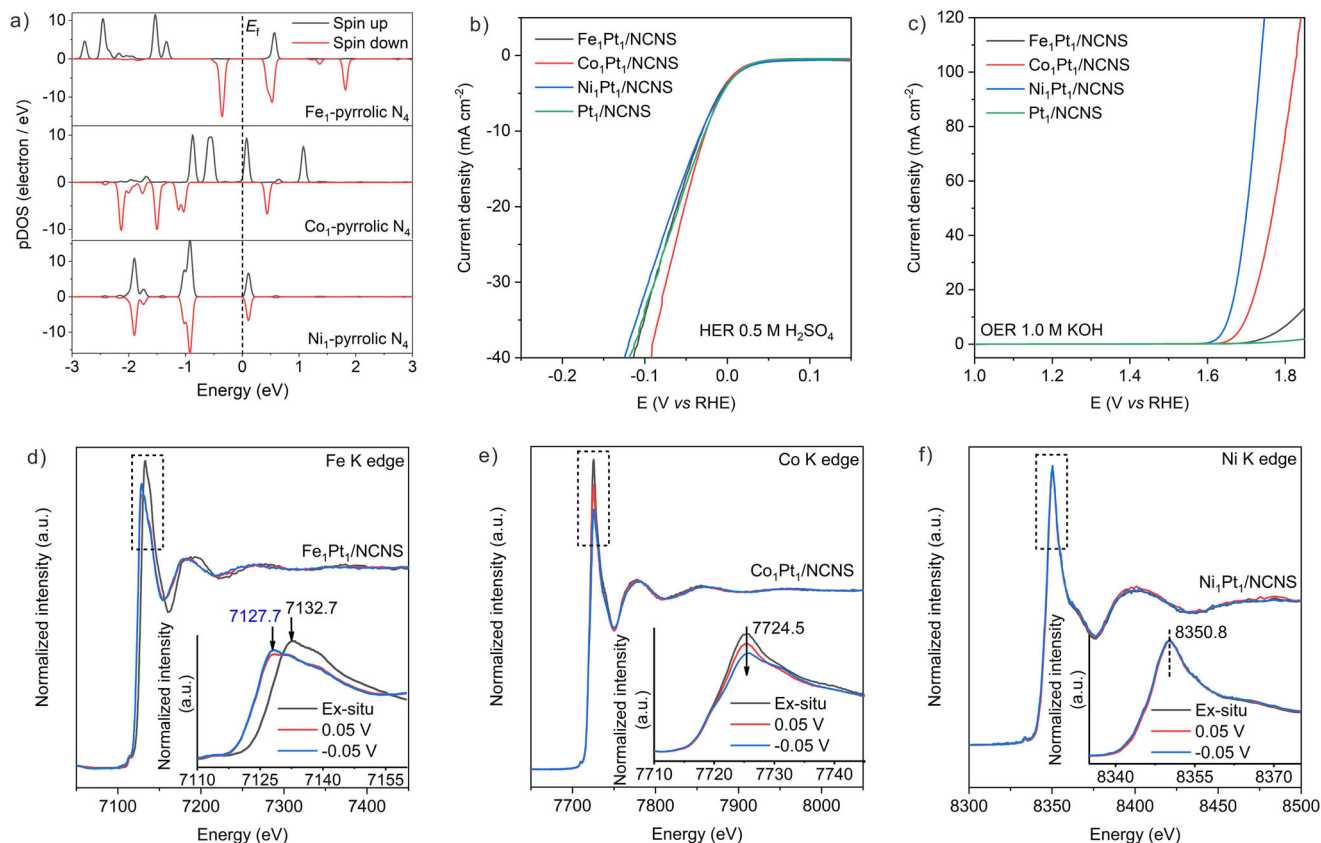


Fig. 6 Theoretical and experimental electrocatalytic analysis on $M_1Pt_1/NCNS$ ($M=Co, Fe, \text{ and } Ni$). **a** Projected density of state (pDOS) on the M_1 3d orbitals with the Fermi level set at zero. HER (**b**) and OER (**c**) LSV curves of $M_1Pt_1/NCNS$ and $Pt_1/NCNS$ with IR correction. **d–f** Operando XANES study on $M_1Pt_1/NCNS$ catalysts in HER working conditions under different potentials at Fe, Co, and Ni K edges, respectively. Inserts: the enlarged area of XANES region in the dash square.

density of state (pDOS) of various M_1 -pyrrolic N_4 sites. As shown in Fig. 6a, the Co_1 -pyrrolic N_4 and Fe_1 -pyrrolic N_4 show higher DOS near the Fermi level than that of Ni_1 -pyrrolic N_4 . As is known, the high electron densities near the Fermi level could facilitate the adsorption of the proton (H^+)^{41–43}. Further calculated hydrogen adsorption free energy on Co_1 -pyrrolic N_4 catalyst is closer to zero than that on Fe_1 -pyrrolic N_4 , indicating its relatively higher catalytic performance in HER (Supplementary Fig. 21). The Ni_1 -pyrrolic N_4 shows the weakest H adsorption ability, indicating its unsatisfactory HER activity. This theoretical prediction is confirmed by the experiment, in which the $Co_1Pt_1/NCNS$ showed higher activity than $Fe_1Pt_1/NCNS$ and $Ni_1Pt_1/NCNS$ (Fig. 6b). The higher catalytic activity of $Co_1Pt_1/NCNS$ than the $Pt_1/NCNS$ could be attributed to the contributions of Co_1 atoms in HER (Supplementary Figs. 22 and 23)^{44–46}. The $Co_1Pt_1/NCNS$ also exhibits good stability without showing any obvious activity decrease after 8,000 cycles durability test (Supplementary Fig. 24). Although the Ni_1 -pyrrolic N_4 site exhibits low catalytic activity in HER, the high d -band center near the Fermi level on the Ni_1 atom (Fig. 6a and Supplementary Table 4) shows the promising application in OER⁴⁷. In the experiment, the $Ni_1Pt_1/NCNS$ shows the best catalytic performance among various SACs in OER (Fig. 6c), which confirms the theoretical prediction (Supplementary Figs. 25 and 26). The NCNS shows no catalytic activity in OER, indicating the carbon corrosion is not obvious (Supplementary Fig. 27).

The non-noble SACs are reported to show promising HER performance but the nature of active sites under HER has not been systematically investigated yet. Therefore, in order to better understand the nature of single-atom sites under reaction,

operando XAS experiments were conducted on $M_1Pt_1/NCNS$ under HER at Fe, Co, and Ni K edges, respectively (Supplementary Fig. 28). As shown in Fig. 6d, a distinct energy chemical shift in the XANES white-line (WL) region can be observed on $Fe_1Pt_1/NCNS$ at Fe K edge from 7132.7 to 7127.7 eV when the overpotential is applied on 0.05 V. This operando XANES results indicate the reduced oxidation state of Fe from +3 to +2. This $Fe^{3+}(d^5)/Fe^{2+}(d^6)$ redox transition is probably from the desorption of covered O species or impressed voltage, which would lead to a distorted $Fe^{2+}-N_4$ structure^{40,48}. As shown in Fig. 6e, an obvious WL intensity decrease can be found on the $Co_1Pt_1/NCNS$ at Co K edge with the increasing overpotentials. Unlike the results of Fe (Supplementary Fig. 29a), the E_0 on the Co K edge keeps constant (Supplementary Fig. 29b). This decreased WL intensity indicates the filling of p electrons on Co, which could play an important role in the HER. The constant E_0 is likely from the charge redistribution from the hybridization among atomic orbitals in Co, which results in the negligible net effect on E_0 . In sharp contrast with the operando XANES results on Fe_1 and Co_1 atoms, neither the E_0 nor the WL intensity on Ni K edge of Ni_1 atoms showed obvious changes (Fig. 6f and Supplementary Fig. 29c), indicating the Ni_1 -pyrrolic N_4 sites may be intact under HER. We also measured the operando XANES on the Fe, Co, and Ni -NPs/NCNS under HER for comparison, where no changes can be found on all the spectra (Supplementary Fig. 30). These apparently insensitive responses under electrochemical reactions might account for their poor activity in HER (Supplementary Fig. 31).

For the first time, the synthesis of M_1 -pyrrolic N_4 type SACs has been successfully achieved using heterogeneously supported Pt_1

atoms as catalysts. This general M_1 -pyrrolic N_4 framework is confirmed by XANES simulation and EXAFS analysis. DFT calculations show that the Pt_1 atoms act as the catalyst to modulate the adsorption behavior and promote the dissociation of $Co(Cp)_2$ in Co ALD, which leads to the chemical binding of $CoCp$ on the pyrrolic N_4 site and formation of Co single atoms. More importantly, this synthesis strategy can be extended to achieve Fe and Ni SACs. These SACs are evaluated under HER and the nature of single-atom sites are further unveiled by the operando XAS studies. In OER, the $Ni_1Pt_1/NCNS$ catalyst show much better catalytic activity than the Fe and Co SACs counterparts, which is in excellent agreement with DFT prediction. These new findings extend the application fields of SACs to catalytic fabrication methodology, which is promising for the rational design of advanced SACs. The prominent covalent metal-support interaction bonding of M_1 atom ($M=Fe, Co, Ni$) with the local coordinated N-atoms provides a unique opportunity to further tune the catalytic properties through substrate design^{49,50}.

Methods

Synthesis of $g-C_3N_4$. Twelve grams of urea was put into an alumina crucible with a cover and then heated to 580 °C at a rate of 3 °C/min in a muffle furnace and maintained at this temperature for 4 h. After cooling down to room temperature, ~600 mg of bulk $g-C_3N_4$ was obtained.

Synthesis of N-doped carbon nanosheet. The synthesis method for the N-doped carbon nanosheets is based on a previous report³⁴. Typically, 500 mg $g-C_3N_4$ was mixed with 2.16 g glucose and dispersed in 40 mL of deionized water under sonication for 5 h. After that, the suspension was transferred to a Teflon autoclave and heated at 140 °C for 11 h in an oven. The product was collected by centrifugation and washed with water and ethanol several times, then dried under vacuum at 60 °C overnight. After that, the dried powder was heated up to 900 °C in Ar at a rate of 5 °C/min and maintained at this temperature for 1 h to achieve the N-doped carbon nanosheet (NCNS).

Synthesis of $Pt_1/NCNS$. Pt was deposited on the as-prepared NCNS by ALD (Savannah 100, Cambridge Nanotechnology Inc., USA) using trimethyl(methylcyclopentadienyl)-platinum (IV) ($MeCpPtMe_3$) and O_2 as precursors. High-purity N_2 (99.9995%) was used as both a purging gas and carrier gas. The deposition temperature was kept at 150 °C, while the container for $MeCpPtMe_3$ was heated to 65 °C to provide a steady flux of Pt to the reactor. The manifold was kept at 115 °C to avoid any condensation⁵. The timing sequence of one cycle Pt ALD was 15s and 30s for $MeCpPtMe_3$ exposure and N_2 purge respectively. Subsequently, the ALD chamber was heated up to 250 °C, with 30s O_2 exposure and 30s N_2 purge to remove the ligand.

Synthesis of $M_1Pt_1/NCNS$ ($M=Fe, Co, and Ni$). The M ALD is conducted on the as-prepared $Pt_1/NCNS$. The precursor used for Co, Fe and Ni are Ferrocene ($Fe(Cp)_2$), Cobaltocene ($Co(Cp)_2$) and Nickelocene ($Ni(Cp)_2$). High-purity N_2 (99.9995%) was used as both a purging gas and carrier gas. The deposition temperature was kept at 250 °C, while the container for $M(Cp)_2$ was heated to 90 °C to provide a steady flux of precursor to the reactor. The manifold was kept at 140 °C to avoid any condensation. The timing sequence of one cycle M ALD was 15s and 30s for $M(Cp)_2$ exposure and N_2 purge respectively. Subsequently, the ALD chamber was heated up to 300 °C, with 30s O_2 exposure and 30s N_2 purge to remove the ligand.

Instrumentation. TEM samples were prepared by drop-casting an ultrasonicated solution of dilute high-performance liquid chromatography grade methanol solution with the sample of interest onto a lacey carbon grid. The TEM characterization was carried out on a FEI Titan Cubed 80–300 kV microscope equipped with spherical aberration correctors (for probe and image forming lenses) at 200 kV. Atomic-resolution high-angle annular dark-field scanning transmission electron microscopy (HAADF-STEM) images were taken using a double spherical aberration-corrected FEI Themis microscope operated at 300 kV. The corresponding inner and outer collection semi-angles for HAADF imaging were 48–200 mrad. Dual EELS spectrum imaging was performed at a collection semi-angle of 28.7 mrad with a dispersion of 0.5 eV/channel. The metal loadings were analyzed using an inductively coupled plasma optical emission spectrometer (ICP-OES) with samples dissolved in hot fresh aqua regia overnight and filtered.

Electrochemical measurements. The electrochemical measurements were performed using a glassy carbon rotating-disk electrode (Pine Instruments) as the working electrode with carbon paper and a standard hydrogen electrode as the counter and reference electrodes, respectively. Ink for the electrochemical measurement was

prepared by adding 2 mg of the catalyst into 1 mL ethanol, and Nafion (5% solution, Sigma-Aldrich, 20 μ L), followed by sonication for 10 min. A working electrode was prepared by loading the ink (10 μ L) on the glassy carbon electrode. The HER test was carried out in 0.5 M H_2SO_4 with a scan rate of 0.01 $V s^{-1}$. The durability test was carried out in 0.5 M H_2SO_4 between –0.1 and 0.4 V at a scan rate of 0.1 $V s^{-1}$. The OER LSV polarization curves were measured in a O_2 -saturated electrolyte at a sweep rate of 5 $mV s^{-1}$. The durability test was carried out on a constant current density of 10 mA/cm^2 . The measured potential against the reference electrode was converted to a reversible hydrogen electrode (RHE).

XAS measurements. XAS measurements were conducted on the 061D superconducting wiggler at the hard X-ray microanalysis (HXMA) beamline at the Canadian Light Source (CLS) and beamline 20-ID-C at the CLS@APS of the Advanced Photon Source (APS), Argonne National Laboratory (ANL).

At HXMA beamline, each spectrum was collected using fluorescence yield mode with a Canberra 32 element Ge detector. The beamline initial energy calibration for the different edges was made by using the corresponding metallic foils from Exafs Materials, and the same metallic foil was further set between two FMB Oxford ion chamber detectors downstream to the sample, making in-step energy calibration available for each individual XAFS scan.

At 20-ID-C beamline, the XAS measurements were conducted at A Si (111) fixed-exit, double-crystal monochromator was used. Harmonic rejection was facilitated by detuning the beam intensity 15% at ~1000 eV above the edge of interest. The measurements were performed in fluorescence mode using a four-element Vortex Si Drift detector. Details on the beamline optics and instruments can be found elsewhere⁵¹.

Operando XAFS measurements were performed with catalyst-coated carbon paper using a custom-built cell. The carbon paper was pretreated with concentrated nitric acid at 80 °C overnight to ensure thorough electrolyte wetting. The catalyst ink was prepared with the same method as for the electrochemical measurements. The catalyst ink was dropped onto the carbon paper, and the backside of the carbon paper was taped with the Kapton film as the working electrode to ensure the entirety of the electrocatalyst had access to the H_2SO_4 electrolyte. Carbon paper and Ag/AgCl were used as the counter and reference electrodes. To collect the XAFS spectra during the HER process, the cathodic voltages were held at constant potentials during the operando experiment from 0.05 to –0.05 V (vs RHE), respectively.

XANES modeling. To further understand the nature of experimental resolved XANES features and address them to the structural and chemical nature of M (Fe, Co, and Ni) site occupancy and their corresponding local structural environment, DFT guided XANES theoretical modeling was carried out by using code FDMNES, following standard procedure⁵². For instance, a Co centered cluster was developed based on the structure model predicated by DFT optimized structures. The radius of the cluster is around 6 Å, corresponding roughly to the detection limit of the XAFS data.

EXAFS data analysis. The data reduction was using codes Athena⁵³. The followed EXAFS R space curve fitting was performed using WINXAS version 2.3, following the procedure reported reference⁵⁴. In brief, the first inflection point of the XANES edge was defined as the experimental E_0 , the post-absorption edge background was estimated and removed by cubic spline fits. Based on the local structural environment predicted by DFT theoretical modeling, the scattering amplitudes and phases were calculated using FEFF7.02 and further used for R space curve fitting⁵⁵. The k ranges for FT-EXAFS for Pt L₃, Fe, Co, and Ni K edges are 3.15–11.57, 2.50–11.16, 2.37–10.90, and 2.33 to 10.48 Å⁻¹, respectively.

Theoretical and computational methods. First-principles DFT calculations were performed by using the spin-polarized Kohn–Sham formalism with the generalized gradient approximation (GGA) of Perdew–Burke–Ernzerhof (PBE)⁵⁶, as implemented in the Vienna ab initio Simulation Package (VASP 5.4.4)⁵⁷. The valence electronic states of all atoms were expanded in plane-wave basis sets with a cutoff energy of 400 eV, and gamma points were used for Brillouin zone integration. All atoms were allowed to relax until the forces fell below 0.02 eV Å⁻¹. The energy convergence criterion was set to 10⁻⁵ eV. The zero-point vibrational energy (ZPE) and entropy corrections were performed by vibrational frequency analysis. We applied a graphene supercell with the surface periodicity of 8 × 8 including 128 atoms as a basis to construct the M-pyrrolic N_4 moieties. A vacuum region of 15 Å in the normal direction of the graphene plane was created to ensure negligible interaction between mirror images of the supercells.

Data availability

The data that support the findings of this study are available from the corresponding author upon reasonable request.

Received: 16 March 2021; Accepted: 25 October 2021;

Published online: 23 November 2021

References

1. Qiao, B. et al. Single-atom catalysis of CO oxidation using Pt₁/FeOx. *Nat. Chem.* **3**, 634–641 (2011).
2. Cao, L. N. et al. Atomically dispersed iron hydroxide anchored on Pt for preferential oxidation of CO in H₂. *Nature* **565**, 631–635 (2019).
3. Yan, H. et al. Single-Atom Pd₁/graphene catalyst achieved by atomic layer deposition: remarkable performance in selective hydrogenation of 1,3-butadiene. *J. Am. Chem. Soc.* **137**, 10484–10487 (2015).
4. Yan, H. et al. Bottom-up precise synthesis of stable platinum dimers on graphene. *Nat. Commun.* **8**, 1070 (2017).
5. Li, J. et al. Highly active and stable metal single-atom catalysts achieved by strong electronic metal–support interactions. *J. Am. Chem. Soc.* **141**, 14515–14519 (2019).
6. Wang, Q. et al. Ultrahigh-loading of Ir single atoms on NiO matrix to dramatically enhance oxygen evolution reaction. *J. Am. Chem. Soc.* **142**, 7425–7433 (2020).
7. Zhao, D. et al. Atomic site electrocatalysts for water splitting, oxygen reduction and selective oxidation. *Chem. Soc. Rev.* **49**, 2215–2264 (2020).
8. Fan, L. L. et al. Atomically isolated nickel species anchored on graphitized carbon for efficient hydrogen evolution electrocatalysis. *Nat. Commun.* **7**, 10667 (2016).
9. Cheng, N., Zhang, L., Doyle-Davis, K. & Sun, X. Single-atom catalysts: from design to application. *Electrochem. Energy Rev.* **2**, 539–573 (2019).
10. Yang, X. F. et al. Single-atom catalysts: a new frontier in heterogeneous catalysis. *Acc. Chem. Res.* **46**, 1740–1748 (2013).
11. Zhuo, H.-Y. et al. Theoretical understandings of graphene-based metal single-atom catalysts: stability and catalytic performance. *Chem. Rev.* **120**, 12315–12341 (2020).
12. Kaiser, S. K., Chen, Z., Faust Akl, D., Mitchell, S. & Pérez-Ramírez, J. Single-atom catalysts across the periodic table. *Chem. Rev.* **120**, 11703–11809 (2020).
13. Ji, S. et al. Chemical synthesis of single atomic site catalysts. *Chem. Rev.* **120**, 11900–11955 (2020).
14. Lang, R. et al. Single-atom catalysts based on the metal–oxide interaction. *Chem. Rev.* **120**, 11986–12043 (2020).
15. Du, Z. et al. Cobalt in nitrogen-doped graphene as single-atom catalyst for high-sulfur content lithium–sulfur batteries. *J. Am. Chem. Soc.* **141**, 3977–3985 (2019).
16. Wang, A., Li, J. & Zhang, T. Heterogeneous single-atom catalysis. *Nat. Rev. Chem.* **2**, 65–81 (2018).
17. Lee, B.-H. et al. Reversible and cooperative photoactivation of single-atom Cu/TiO₂ photocatalysts. *Nat. Mater.* **18**, 620–626 (2019).
18. Zhou, M. et al. Single-atom Ni-N₄ provides a robust cellular NO sensor. *Nat. Commun.* **11**, 3188 (2020).
19. Duchesne, P. N. et al. Golden single-atomic-site platinum electrocatalysts. *Nat. Mater.* **17**, 1033–1039 (2018).
20. Vilé, G. et al. A stable single-site palladium catalyst for hydrogenations. *Angew. Chem. Int. Ed.* **54**, 11265–11269 (2015).
21. Kistler, J. D. et al. A single-site platinum CO oxidation catalyst in zeolite KLTL: microscopic and spectroscopic determination of the locations of the platinum atoms. *Angew. Chem. Int. Ed.* **53**, 8904–8907 (2014).
22. Chen, Y. et al. Discovering partially charged single-atom Pt for enhanced anti-markovnikov alkene hydrosilylation. *J. Am. Chem. Soc.* **140**, 7407–7410 (2018).
23. Liu, Y. et al. A general strategy for fabricating isolated single metal atomic site catalysts in Y zeolite. *J. Am. Chem. Soc.* **141**, 9305–9311 (2019).
24. Han, A. et al. Recent advances for MOF-derived carbon-supported single-atom catalysts. *Small Methods* **3**, 1800471 (2019).
25. Jones, J. et al. Thermally stable single-atom platinum-on-ceria catalysts via atom trapping. *Science* **353**, 150–154 (2016).
26. Lang, R. et al. Non defect-stabilized thermally stable single-atom catalyst. *Nat. Commun.* **10**, 234 (2019).
27. Yao, Y. et al. High temperature shockwave stabilized single atoms. *Nat. Nanotechnol.* **14**, 851–857 (2019).
28. Wang, X. et al. Supported single Fe atoms prepared via atomic layer deposition for catalytic reactions. *ACS Appl. Nano Mater.* **3**, 2867–2874 (2020).
29. Cao, Y. et al. Atomic-level insight into optimizing the hydrogen evolution pathway over a Co₁-N₄ single-site photocatalyst. *Angew. Chem. Int. Ed.* **56**, 12191–12196 (2017).
30. Karasulu, B., Vervuurt, R. H., Kessels, W. M. & Bol, A. A. Continuous and ultrathin platinum films on graphene using atomic layer deposition: a combined computational and experimental study. *Nanoscale* **8**, 19829–19845 (2016).
31. Lu, J., Elam, J. W. & Stair, P. C. Atomic layer deposition-sequential self-limiting surface reactions for advanced catalyst “bottom-up” synthesis. *Surf. Sci. Rep.* **71**, 410–472 (2016).
32. Wang, H., Wang, C., Yan, H., Yi, H. & Lu, J. Precisely-controlled synthesis of Au@Pd core-shell bimetallic catalyst via atomic layer deposition for selective oxidation of benzyl alcohol. *J. Catal.* **324**, 59–68 (2015).
33. Martensson, P. & Carlsson, J.-O. Atomic layer epitaxy of copper-Growth and selectivity in the Cu (II)-2, 2, 6, 6-tetramethyl-3, 5-heptanedionate/H₂ process. *J. Electrochem. Soc.* **145**, 2926–2931 (1998).
34. Yu, H. et al. Nitrogen-doped porous carbon nanosheets templated from g-C₃N₄ as metal-free electrocatalysts for efficient oxygen reduction reaction. *Adv. Mater.* **28**, 5080–5086 (2016).
35. Li, L. et al. Tailoring selectivity of electrochemical hydrogen peroxide generation by tunable pyrrolic-nitrogen-carbon. *Adv. Energy Mater.* **10**, 2000789 (2020).
36. Li, J. et al. Unveiling the nature of Pt single-atom catalyst during electrocatalytic hydrogen evolution and oxygen reduction reactions. *Small* **17**, 2007245 (2021).
37. Choi, J. & Dowben, P. A. Cobaltocene adsorption and dissociation on Cu (1 1 1). *Surf. Sci.* **600**, 2997–3002 (2006).
38. Yan, H. et al. Atomic engineering of high-density isolated Co atoms on graphene with proximal-atom controlled reaction selectivity. *Nat. Commun.* **9**, 3197 (2018).
39. Zitolo, A. et al. Identification of catalytic sites in cobalt-nitrogen-carbon materials for the oxygen reduction reaction. *Nat. Commun.* **8**, 957 (2017).
40. Jia, Q. et al. Experimental observation of redox-induced Fe–N switching behavior as a determinant role for oxygen reduction activity. *ACS Nano* **9**, 12496–12505 (2015).
41. Zhang, L. et al. Graphene defects trap atomic Ni species for hydrogen and oxygen evolution reactions. *Chem* **4**, 285–297 (2018).
42. Chen, W. et al. Rational design of single molybdenum atoms anchored on N-doped carbon for effective hydrogen evolution reaction. *Angew. Chem. Int. Ed.* **56**, 16086–16090 (2017).
43. Ye, S. et al. Highly stable single Pt atomic sites anchored on aniline-stacked graphene for hydrogen evolution reaction. *Energy Environ. Sci.* **12**, 1000–1007 (2019).
44. Zhang, L. Z. et al. Charge polarization from atomic metals on adjacent graphitic layers for enhancing the hydrogen evolution reaction. *Angew. Chem. Int. Ed.* **58**, 9404–9408 (2019).
45. Zhang, L. Z. et al. Coordination of atomic Co-Pt coupling species at carbon defects as active sites for oxygen reduction reaction. *J. Am. Chem. Soc.* **140**, 10757–10763 (2018).
46. Zhuang, L. et al. Defect-Induced Pt–Co–Se coordinated sites with highly asymmetrical electronic distribution for boosting oxygen-involving electrocatalysis. *Adv. Mater.* **31**, 1805581 (2019).
47. Montemore, M. M., van Spronsen, M. A., Madix, R. J. & Friend, C. M. O₂ activation by metal surfaces: implications for bonding and reactivity on heterogeneous catalysts. *Chem. Rev.* **118**, 2816–2862 (2017).
48. Li, J. et al. Structural and mechanistic basis for the high activity of Fe–N–C catalysts toward oxygen reduction. *Energy Environ. Sci.* **9**, 2418–2432 (2016).
49. Qiao, B. et al. Ultrastable single-atom gold catalysts with strong covalent metal-support interaction (CMSI). *Nano Res.* **8**, 2913–2924 (2015).
50. Liu, J.-C., Tang, Y., Wang, Y.-G., Zhang, T. & Li, J. Theoretical understanding of the stability of single-atom catalysts. *Natl. Sci. Rev.* **5**, 638–641 (2018).
51. Heald, S., Cross, J., Brewster, D. & Gordon, R. The PNC/XOR X-ray microprobe station at APS sector 20. *Nucl. Instrum. Methods Phys. Res.* **582**, 215–217 (2007).
52. Joly, Y. X-ray absorption near-edge structure calculations beyond the muffin-tin approximation. *Phys. Rev. B* **63**, 125120 (2001).
53. Ravel, B. & Newville, M. ATHENA, ARTEMIS, HEPHAESTUS: data analysis for X-ray absorption spectroscopy using IFEFFIT. *J. Synchrotron Radiat.* **12**, 537–541 (2005).
54. Ressler, T. WinXAS: A new software package not only for the analysis of energy-dispersive XAS data. *J. Phys. IV* **7**, C2-269–C262–C2-26270 (1997).
55. Rehr, J. J. & Albers, R. C. Theoretical approaches to x-ray absorption fine structure. *Rev. Mod. Phys.* **72**, 621 (2000).
56. Perdew, J. P., Burke, K. & Ernzerhof, M. Generalized gradient approximation made simple. *Phys. Rev. Lett.* **77**, 3865 (1996).
57. Kresse, G. & Furthmüller, J. Efficient iterative schemes for ab initio total-energy calculations using a plane-wave basis set. *Phys. Rev. B* **54**, 11169 (1996).

Acknowledgements

This work was supported by the Natural Sciences and Engineering Research Council of Canada (NSERC), Ballard Power Systems, Canada Research Chair (CRC) Program, Canada Foundation for Innovation (CFI), the University of Western Ontario, and the 111 Project of China (D17003). Junjie Li was supported by the China Scholarship Council (CSC). Jun Li and C.-Q.X. acknowledge financial support from the National Natural Science Foundation of China (No. 22033005 and 22038002). This work was partially sponsored by the Guangdong Provincial Key Laboratory of Catalysis (No. 2020B121201002). Computational resources are supported by the Center for Computational Science and Engineering (SUSTech). This STEM work was supported by the National Natural Science Foundation of China (No. 21802065) and the Pico Center at SUSTech CRF that receives support from the Presidential fund and Development and Reform Commission of Shenzhen Municipality. This research used resources of the

Advanced Photon Source, an Office of Science User Facility operated for the U.S. Department of Energy (DOE) Office of Science by Argonne National Laboratory and was supported by the U.S. DOE under Contract No. DE-AC02-06CH11357, and the Canadian Light Source and its funding partners. The authors also would like to thank Dr. Timothy Fister for the use of the electrochemical workstation during the *operando* experiments at APS.

Author contributions

Junjie Li and X.S. designed the project. Junjie Li performed the catalyst preparation, catalytic tests, XAS experiment, and wrote the manuscript; Y.J., C.X., and J. Li performed the DFT calculations. Q.W., D.W., and M.G. conducted the HAADF-STEM images acquisition and image analyses; N.C. carried out the XANES and EXAFS data analysis. M.N.B., K.A., K.D., D.M.M., Z.F., and W.L. assisted to run the XAS experiment; L.Z., R.L., and T.-K.S. gave constructive suggestions; X.S. supervised the project. All authors reviewed the manuscript.

Competing interests

The authors declare no competing interests.

Additional information

Supplementary information The online version contains supplementary material available at <https://doi.org/10.1038/s41467-021-27143-5>.

Correspondence and requests for materials should be addressed to Ning Chen, Meng Gu, Jun Li or Xueliang Sun.

Reprints and permission information is available at <http://www.nature.com/reprints>

Publisher's note Springer Nature remains neutral with regard to jurisdictional claims in published maps and institutional affiliations.



Open Access This article is licensed under a Creative Commons Attribution 4.0 International License, which permits use, sharing, adaptation, distribution and reproduction in any medium or format, as long as you give appropriate credit to the original author(s) and the source, provide a link to the Creative Commons license, and indicate if changes were made. The images or other third party material in this article are included in the article's Creative Commons license, unless indicated otherwise in a credit line to the material. If material is not included in the article's Creative Commons license and your intended use is not permitted by statutory regulation or exceeds the permitted use, you will need to obtain permission directly from the copyright holder. To view a copy of this license, visit <http://creativecommons.org/licenses/by/4.0/>.

© The Author(s) 2021